# Rashba-split image-potential state and unoccupied surface electronic structure of Re(0001)

Fabian Schöttke,[1,*] Sven Schemmelmann,[1] Peter Krüger,[2] and Markus Donath[1,†]

[1]*Physikalisches Institut, Westfälische Wilhelms-Universität Münster, Wilhelm-Klemm-Straße 10, 48149 Münster, Germany*

[2]*Institut für Festkörpertheorie, Westfälische Wilhelms-Universität Münster, Wilhelm-Klemm-Straße 10, 48149 Münster, Germany*

(Received 10 December 2021; revised 22 February 2022; accepted 15 April 2022; published 27 April 2022)

The influence of spin-orbit interaction on the unoccupied electronic structure of the Re(0001) surface is investigated by spin- and angle-resolved inverse photoemission and density-functional theory calculations. In the two high-symmetry azimuths $\overline{\Gamma}\,\overline{\mathrm{K}}$ and $\overline{\Gamma}\,\overline{\mathrm{M}}$, we identify transitions into $d$-derived bulk states as well as different types of surface states. The Rashba-type spin-split hole pocket around $\overline{\Gamma}$ finds continuation in empty spin-split surface states for higher $\mathbf{k}_\parallel$, thereby forming W-shaped states whose lower parts are partially occupied. A large energy gap below and above the vacuum energy around $\overline{\Gamma}$ hosts image-potential-induced surface states. The $n = 1$ member of the Rydberg-like series exhibits a free-electron-like $E(\mathbf{k}_\parallel)$ dispersion with an effective mass of $m^*/m_e = 1.2 \pm 0.1$. Careful spin-resolved measurements for several angles of electron incidence allow us to detect Rashba-type spin-dependent energy splittings of this state with a Rashba parameter of $\alpha_\mathrm{R} = 105 \pm 33$ meV Å.

DOI: 10.1103/PhysRevB.105.155419

## I. INTRODUCTION

The influence of spin-orbit interaction (SOI) on the electronic structure of solids and surfaces has been extensively studied theoretically as well as experimentally [1–3]. Prototypical examples of elements with a high atomic number $Z$, where strong SOI-induced effects are expected, are found in the sixth period of the periodic table. Detailed studies on the surfaces of Ir, Pt, and Au (fcc structure) [4–8] and Ta and W (bcc structure) [9–16] provided a wealth of information about the spin dependence of surface states caused by the broken inversion symmetry at the surface. Not only Shockley- and Tamm-type states in gaps of the projected bulk band structure but also topologically nontrivial Dirac-type states in SOI-induced energy gaps have been experimentally observed and theoretically described [17–19]. Less is known about two further elements of the sixth period, but with hcp crystal structure, namely, Re and Os. Recently, theoretical studies reported on spin-orbit-influenced surface states at these surfaces [20,21]. The first spin-resolved (inverse) photoemission studies for Re(0001) confirmed the existence of occupied and unoccupied surface states around $\overline{\Gamma}$ [22,23].

Besides the already mentioned types of surface states, there is an additional class that is caused by the long-range Coulomb-like surface barrier potential at the surface of conductive materials, called image-potential-induced surface states or, in short, image states [24,25]. They form a Rydberg-like series of states, pinned to the vacuum level within less than 1 eV. As a consequence, these states are unoccupied and cannot be investigated by conventional photoemission. Inverse photoemission (IPE) and two-photon photoemission (2PPE) have been successfully used to study their binding energy, their energy vs momentum dispersion, and their lifetimes [26–28].

Since image states are located mainly in the vacuum in front of the surface, the influence of spin-dependent interactions on these states is a topic of ongoing debate in the literature. It is well established that exchange interaction in ferromagnets causes exchange splittings in image states [29]. The size of the exchange splitting is about a factor of 10 smaller than the splitting of the magnetic bands due to the small overlap of image states with bulk states.

Much less is known about the influence of spin-orbit interaction on image states at the surface of high-$Z$ materials. The atomic potential gradient which corresponds to spin-orbit coupling is well described by density-functional theory (DFT) calculations. Employing a model potential with the correct $1/z$ behavior outside the solid in these computations, McLaughlan *et al.* predicted Rashba-type spin-orbit splittings of image states at Ir, Pt, and Au surfaces [30]. Following the seminal paper by Bychkov and Rashba [31], a quantitative measure of the Rashba effect in free-electron-like systems with effective mass $m^*$ is given by the so-called Rashba parameter $\alpha_\mathrm{R}$:

$$E_\pm(\mathbf{k}_\parallel) = \hbar^2\mathbf{k}_\parallel^2/2m^* \pm \alpha_\mathrm{R}|\mathbf{k}_\parallel|.$$

The Rashba parameters $\alpha_\mathrm{R}$ for image states on the above-mentioned surfaces were predicted to be in the range of 19–44 meV Å [30]. These values are about a factor of 10 smaller than for the prototypical Rashba-split $L$-gap surface state on Au(111) [4,32]. A recent theoretical study investigated the impact of SOI on the image states of the high-$Z$ materials Ir(111), Pt(111), Au(001), and $Bi_2Se_3$(0001) [33].

On the experimental side, a Rashba-type spin splitting in the $n = 1$ image state on the graphene/Ir(111) surface was deduced from monochromatic 2PPE using circular dichroism (CD-2PPE) [34]. This result, however, was controversially

*fabian.schoettke@uni-muenster.de
†markus.donath@uni-muenster.de

 

discussed in the literature [35,36]. A further study, again with CD-2PPE but with bichromatic excitation, investigated the image state on Au(001)-(5 × 20): A Rashba parameter of $48^{+8}_{-20}$ meV Å was deduced [37,38]. Note that nonzero CD signals do not directly reflect the spin texture [39,40]. Only with the aid of calculations can the influence of orbital angular momenta and spin texture on the CD signal be evaluated. For this purpose, detailed theoretical information about the orbital composition of the states under investigation is needed. This approach was used in Ref. [37]. Direct experimental access to the spin texture, however, is available by spin-resolved photoemission techniques, i.e., spin-resolved IPE or 2PPE in the case of unoccupied image states. This is our motivation to investigate the image state of Re(0001) with spin-resolved IPE.

In this paper, we present a comprehensive spin- and angle-resolved IPE study of Re(0001) in which we identify unoccupied bulk- and surface-related states, including the image state. In our study we make use of angle-dependent photon detection to estimate the orbital symmetry of the respective state and spin resolution to identify the spin character. We compare our experimental data to calculations within DFT in order to classify the observed states and understand their properties.

## II. EXPERIMENTAL AND THEORETICAL METHODS

The experiments were performed in an ultrahigh-vacuum (UHV) apparatus with a base pressure of $< 5 \times 10^{-11}$ mbar. The unoccupied electronic structure was investigated by spin- and angle-resolved IPE [41]. For excitation, we used spin-polarized electrons of variable kinetic energy from a GaAs photocathode with a spin polarization $P$ of about 29% [42]. The transversal spin polarization of the electron beam was oriented in the surface plane and perpendicular to $\mathbf{k}_\parallel$, i.e., the so-called Rashba direction. The incomplete spin polarization of the electron beam was accounted for by normalizing the spin-resolved IPE spectra to 100% electron spin polarization [41,43]. The electron beam impinges on the sample at a defined angle of incidence $\theta$ (with respect to the surface normal) with a diameter of ≈1.5 mm (FWHM) and with a divergence $\Delta\theta_{\mathrm{FWHM}} < 3^\circ$ [42,44]. For detection of the emitted photons, we used four bandpass detectors, C1 to C4, at different photon take-off angles (as described later) with a fixed mean detection energy of $\hbar\omega = 9.9$ eV and an energy window of 330 meV [45–47]. If not stated otherwise, the IPE spectra shown in this paper are sum spectra from all counters that are not masked by the sample (depending on the electron incidence angle). The overall energy resolution (FWHM) of the IPE experiment, including the energy spread of the electron beam, amounts to $\Delta E \approx 400$ meV [48].

The Re(0001) sample, obtained from MaTecK GmbH (Germany), was mounted on a molybdenum sample holder with a tungsten plate touching the sample to avoid alloying with the molybdenum holder. The sample was cleaned by repeated cycles of annealing at 1400 K in an oxygen atmosphere ($2 \times 10^{-8}$ mbar) for several minutes and subsequent flashing to 1800 K without oxygen [23]. The sample was prepared in a separate preparation chamber connected with the analysis chamber for IPE by a UHV sample-transfer system. The sample quality and the reproducibility of the preparation procedure were monitored by low-energy electron diffraction (LEED) for the crystallographic order and Auger electron spectroscopy (AES) for contaminants on the surface. A small to vanishing carbon signal in AES was a sensitive criterion for surface cleanness. LEED experiments showed that the sample consists of stripelike crystallites with a width of at least 2 mm and tilt angles up to 1° between two crystallites [23]. Single-crystalline surface areas were chosen for the position of the incident electron beam for IPE. All IPE measurements were performed at a sample temperature of 300 K.

We have performed calculations within the framework of density-functional theory employing the local density approximation [49]. To this end, the electronic wave functions are represented by a basis set of atomic-centered Gaussian orbitals with $s$, $p$, and $d$ symmetry [50]. Norm-conserving pseudopotentials [51] that include scalar relativistic corrections as well as spin-orbit coupling [52] are used in the Kleinman-Bylander [53] form. The Re(0001) surface is treated within a supercell approach by employing a slab of 40 Re layers. Relaxations on the eight topmost layers have been taken into account. For technical details of these calculations see Ref. [23].

## III. RESULTS AND DISCUSSION

### A. Unoccupied electron states along $\overline{\Gamma}\,\overline{\mathrm{K}}$ and $\overline{\Gamma}\,\overline{\mathrm{M}}$

Figure 1 presents angle-resolved IPE spectra of Re(0001) along $\overline{\Gamma}\,\overline{\mathrm{K}}$ [Fig. 1(a)] and along $\overline{\Gamma}\,\overline{\mathrm{M}}$ [Fig. 1(b)]. Dispersing peak positions in the spectra as a function of the electron incidence angle $\theta$ are marked by thick orange and green lines. The color coding indicates the origin of the transitions: orange for transitions into surface states and green for transitions into bulk-derived states. Based on the spectra alone, this assignment is not possible. However, there are experimental as well as theoretical criteria for classification. We used time-dependent intensity losses due to surface contamination as an experimental criterion (not shown) to identify crystal-induced surface states, labeled SS.

Furthermore, we transferred all unambiguous peak positions of the spectra in Fig. 1 to an $E(\mathbf{k}_\parallel)$ plot, shown in Fig. 2(a). The results of both azimuths are combined in this diagram: $\overline{\Gamma}\,\overline{\mathrm{K}}$ to the right and $\overline{\Gamma}\,\overline{\mathrm{M}}$ to the left, both with positive $k_\parallel$ values. [For Fig. 2(a), we restrict ourselves to peak positions in spectra for positive $\theta$, where many spectra have been measured. The few data for negative $\theta$ resemble the results for positive $\theta$.] Together with the experimental data (orange circles and green squares), Fig. 2(a) contains theoretical results for comparison: the surface-projected bulk band structure (blue shaded areas), a slab calculation (gray lines), and the expectation value of the spin polarization of the Rashba component as red (spin up) and blue (spin down) dots on top of surface-related bands from the slab calculations. Note that, due to the chosen way of presentation, the spin polarization does not switch sign at $\overline{\Gamma}$.

Figure 2(b) presents theoretical results for the orbital composition of the surface-related states. Colored dots indicate the different orbital characters: $d_{z^2}$ (magenta), $d_{xy}$, $d_{x^2-y^2}$ (gold), $d_{xz}$, $d_{yz}$ (green), and $p_z$ (brown). The blue-shaded areas

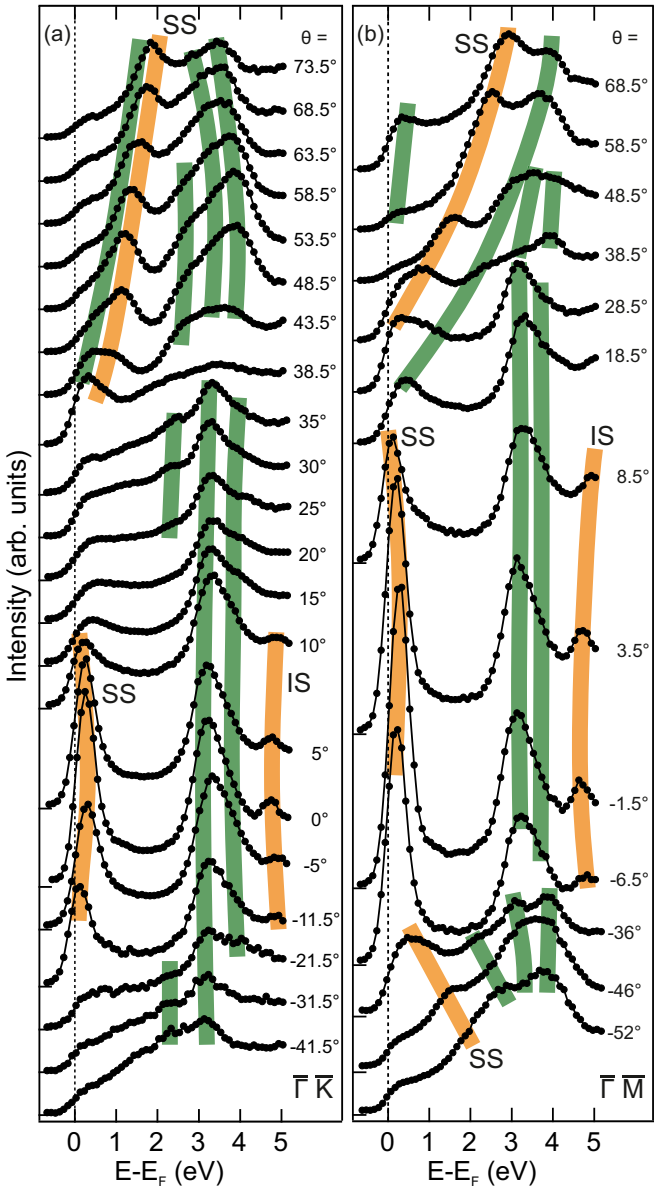


FIG. 1. Angle-resolved IPE spectra for Re(0001) along (a) $\overline{\Gamma}\,\overline{\mathrm{K}}$ and (b) $\overline{\Gamma}\,\overline{\mathrm{M}}$. Green and orange lines connect spectral features originating from transitions into bulk- and surface-derived states, respectively. SS denotes crystal-induced surface states, while IS indicates the image-potential-induced surface state.

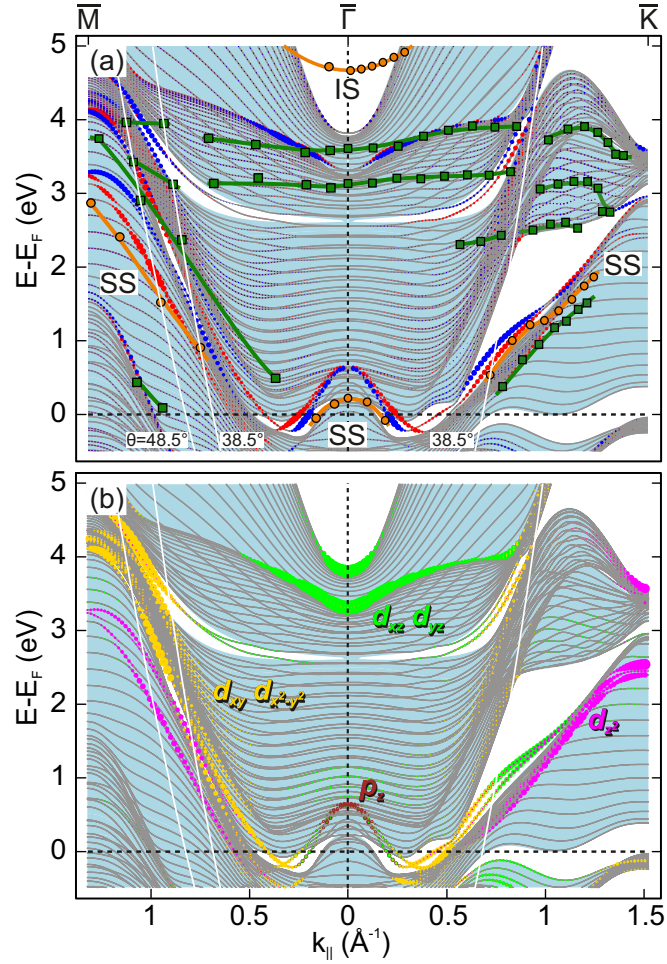


FIG. 2. (a) Energy vs $\mathbf{k}_\parallel$ dispersion of electronic states at Re(0001) along $\overline{\Gamma}\,\overline{\mathrm{M}}$ (left) and along $\overline{\Gamma}\,\overline{\mathrm{K}}$ (right). Green squares and orange circles (connected by colored lines) represent peak positions of the experimental spectra for positive $\theta$ shown in Fig. 1. The blue-shaded areas display the calculated surface-projected bulk band structure; the gray lines are theoretical results of a slab calculation. Red (spin up) and blue (spin down) dots indicate theoretical results for spin-split surface states. The symbol size is proportional to the expectation value of the spin-polarization component in the surface plane and perpendicular to $\mathbf{k}_\parallel$ (Rashba component). (b) Same surface-projected bulk band structure (blue-shaded areas) and results of a slab calculation (gray lines) as in (a), but with surface-related states color-coded with respect to their orbital composition.

(surface-projected bulk band structure) and the gray lines (slab calculations) are the same as in Fig. 2(a). Additional calculations, including transition matrix elements with free electrons as initial states (not shown), indicate that only the bands with $d_{z^2}$ and $p_z$ orbital symmetries can be expected in our IPE spectra with sizable intensities.

Our assignment of the label SS to surface-related bands based on adsorption experiments is supported by theoretical predictions. The down-dispersing state close to $E_\mathrm{F}$ around $\overline{\Gamma}$ originates from the surface state already observed and discussed by photoemission [22] and IPE [23]. In addition, surface-related bands labeled SS with positive dispersion in both azimuthal directions close to gap edges are observed in experiment and theory, but at somewhat lower energies in experiment. The calculations suggest that the down-dispersing SS around $\overline{\Gamma}$ is connected to the up-dispersing SS at higher $k_\parallel$ (within a gap and/or along the gap edge). Both parts together form a W-shaped surface-state structure with slightly different behavior along $\overline{\Gamma}\,\overline{\mathrm{K}}$ and $\overline{\Gamma}\,\overline{\mathrm{M}}$.

One more orange-colored band dispersion appears around $\overline{\Gamma}$ at almost 5 eV above the Fermi level. The energetic position of 4.7 eV at $\overline{\Gamma}$, i.e., about 0.7 eV below the vacuum level (experimentally determined work function $\Phi = 5.34 \pm 0.03$ eV via target-current spectroscopy), the free-electron-like $E(\mathbf{k}_\parallel)$ dispersion, and the less pronounced surface sensitivity compared with SS are clear indications of an

image-potential-induced surface state, which is therefore labeled IS. It lies within a gap of the projected bulk band structure and has no theoretical counterpart in the DFT calculation. Our calculation does not include a long-range surface barrier, which is necessary to describe the IS. We will discuss this state in more detail later.

All remaining spectral features colored in green in both azimuths match $E$-$\mathbf{k}_\parallel$ regions where bulk states exist: (i) the almost flat bands (except at higher $k_\parallel$ along $\overline{\Gamma}\,\overline{\mathrm{K}}$) between 3 and 4 eV above $E_\mathrm{F}$ with a high density of states and (ii) the bands with strong energy dispersion between 0.5 and 1.5 Å$^{-1}$ in regions with a high density of states along gap edges. In the spectra for both azimuths, there is a significant change in the spectral shape for $\theta = 38.5°$. For smaller and larger $\theta$, clear spectral features are observed, while for $\theta = 38.5°$ the spectra are less structured. This is a consequence of the high density of states with strong energy dispersion between 0.5 and 1.0 Å$^{-1}$ in the energy range between 1 and 4 eV. An IPE spectrum measured in the isochromate mode at a fixed photon energy represents an energy distribution curve (EDC) for a given angle of electron incidence $\theta$. Within an $E(\mathbf{k}_\parallel)$ diagram, the EDC follows a parabolic path. In our case, the dispersion behavior of the bands matches this parabolic path (see the white lines in Fig. 2). As a consequence, no clear spectral features can be observed for angles in this range.

As mentioned above, we use several photon counters at different detection angles. In addition, C4 is positioned closer to the sample, thereby collecting photons from a larger solid angle. Comparing the spectral intensities obtained from these counters for the same transition provides additional information about the symmetry of the electron states involved in the dipole transition [54,55].

We explore the photon emission characteristics around $\overline{\Gamma}$ and at $k_\parallel = 0.7$ Å$^{-1}$ along $\overline{\Gamma}\,\overline{\mathrm{K}}$. For the two cases, Fig. 3 shows the photon-detection geometries [Figs. 3(a) and 3(c)] and the corresponding IPE spectra for the individual counters [Figs. 3(b) and 3(d)]. For both angles, no information about the bulk-derived states can be deduced because the spectral intensities are almost independent of the photon detection angle. This is different for the surface states. For almost normal electron incidence [Fig. 3(b)], the intensity of the SS is much lower for C2 and C3 compared with C1 and especially C4; that is, the intensity of the SS is higher for larger detection angles. This is compatible with the assumption of a dipolar axis along the surface normal, which underlines the $\Lambda_6$ symmetry of the $p_z$-derived [see Fig. 2(b)] SS at $\overline{\Gamma}$ [23]. The slightly smaller intensity observed by C1 compared with C4 despite almost identical detection angles may be caused by the small deviation from $\theta = 0$ and the difference in solid angles between C1 and C4.

The dipole-distribution effect for SS is even more pronounced in the spectra for $\theta = 38.5°$ [Fig. 3(d)]. Note that C1 cannot detect any photons in this case because it is masked by the sample. While C3 and C4 detect almost the same notable intensities, negligible intensity is observed by C2. This is a clear indication that the dipolar axis of the transition is oriented along or close to the surface normal, which is pointing directly at C2, again revealing the $z$-type orbital symmetry of the surface state. The experimental result is in agreement with

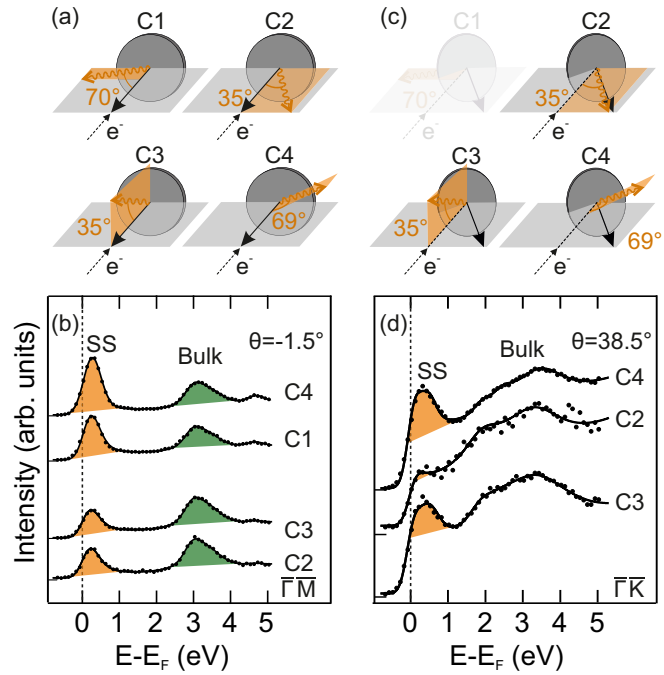


FIG. 3. (a) Photon-detection geometry for counters C1 to C4 for normal electron incidence. The photon-takeoff angles are referenced to the direction of electron incidence (dashed arrow). The black arrow indicates the surface normal. The measurement plane is shown in light gray. (b) IPE spectra for close to normal electron incidence obtained from counters C1 to C4. (c) Same as (a), but for $\theta = 38.5°$. In this case, C1 is masked by the sample. (d) IPE spectra for $\theta = 38.5°$ in the $\overline{\Gamma}\,\overline{\mathrm{K}}$ direction for counters C2 to C4.

the results of our DFT calculation. For $\theta = 38.5°$ ($\overline{\Gamma}\,\overline{\mathrm{K}}$), the calculation predicts surface states with mainly $d_{yz}$ symmetry and surface resonances with $d_{z^2}$ symmetry [see white lines in Fig. 2(b)].

The results of our slab calculation shown in Fig. 2(a) additionally provide information about the spin polarization of the surface-related states. This is true for the surface-state hole pocket around $\overline{\Gamma}$, whose Rashba-type spin polarization was recently confirmed by spin-resolved IPE [23] as well as for the outer branches of the W-shaped surface states with positive $E(\mathbf{k}_\parallel)$ dispersion along or within energy gaps of the projected bulk band structure. This spin-dependent energy splitting is clearly visible in the band gap in $\overline{\Gamma}\,\overline{\mathrm{K}}$ but is largest in the $\overline{\Gamma}\,\overline{\mathrm{M}}$ direction at $k_\parallel \approx 1$ Å$^{-1}$. Along $\overline{\Gamma}\,\overline{\mathrm{M}}$, two spin-split surface-related bands are predicted, one with $d_{xy}$, $d_{x^2-y^2}$ symmetry at higher energies and one with $d_{z^2}$ symmetry at lower energies. As described above, only the latter is expected to appear in our IPE spectra due to symmetry reasons. The theoretically predicted spin splitting amounts to several hundreds of meV.

We performed spin-resolved IPE measurements for almost equivalent positive and negative $\theta$ to test the sign reversal of the spin polarization upon changing the sign of $k_\parallel$. Spin-revolved IPE spectra for 38.5° and −36° as well as for 48.5° and −46° along $\overline{\Gamma}\,\overline{\mathrm{M}}$ are displayed in Figs. 4(a) and 4(b). As expected, we observe one spin-split spectral feature in the energy range of the predicted surface bands. The surface-related spectral emissions labeled SS show, in accordance with the

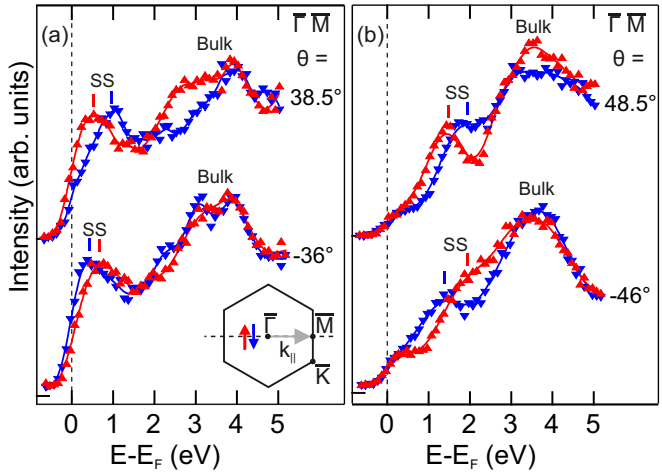


FIG. 4. Spin-resolved IPE spectra of Re(0001) for almost complementary angles of electron incidence, (a) $\theta = 38.5°$ and $-36°$ and (b) $\theta = 48.5°$ and $-46°$, both along $\overline{\Gamma}\,\overline{\mathrm{M}}$. The inset in (a) shows the surface Brillouin zone of Re(0001) with high-symmetry points ($\overline{\Gamma}$, $\overline{\mathrm{K}}$, $\overline{\mathrm{M}}$), the mirror plane (dashed line), and spin-polarization directions (red and blue arrows).

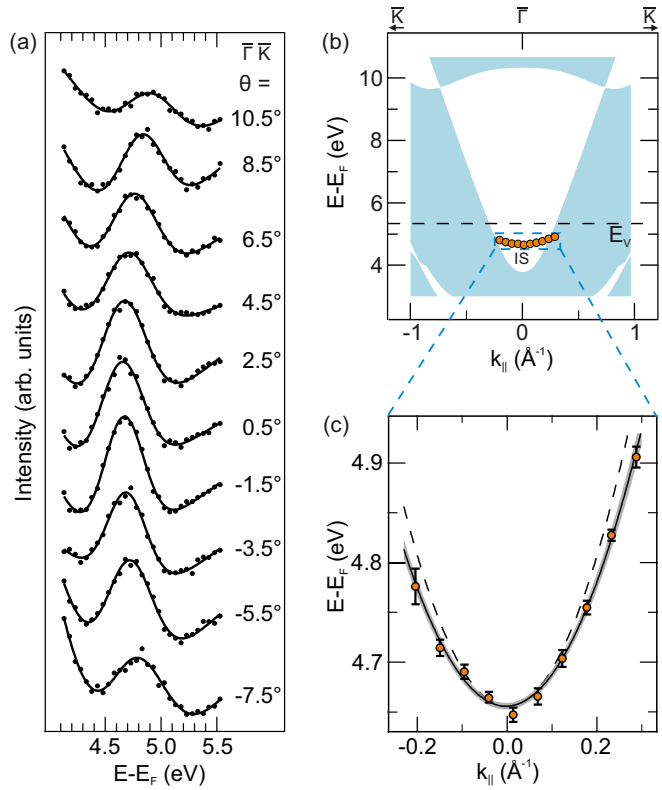


FIG. 5. (a) IPE spectra of the image-potential state IS at Re(0001) for various angles of electron incidence $\theta$ along $\overline{\Gamma}\,\overline{\mathrm{K}}$. Solid lines are fits to the data. (b) $E(\mathbf{k}_{\|})$ dispersion of IS (orange circles) within a gap of the surface-projected bulk band structure (blue-shaded area). The vacuum energy $E_{\mathrm{V}}$ is indicated as a dashed line. (c) Enlargement of (b) with a parabolic fit to the data (black solid line) resulting in an effective mass of $m^*/m_{\mathrm{e}} = 1.2 \pm 0.1$. The gray shading around the black line indicates the $1\sigma$ uncertainty of the fit. For comparison, the dashed line shows the free-electron parabola ($m^*/m_{\mathrm{e}} = 1$).

calculations, a clear Rashba-type spin-dependent energy splitting of several hundreds of meV with sign reversal for positive and negative $\theta$. Since $\overline{\Gamma}\,\overline{\mathrm{M}}$ is a mirror-plane direction, only a Rashba-type spin polarization direction is allowed by symmetry arguments. The bulk-related spectral features also show spin-polarization effects, which are attributed to spin-orbit coupling in bulk continuum states at the surface [56]. For the bulk-related states, the spin asymmetry is not totally reversed upon changing the sign of $k_{\|}$. This may be because of two reasons: (i) Our spectra for positive and negative $k_{\|}$ are not taken at exactly the same $|\theta|$, and (ii) the different photon-detection geometries for $+\theta$ and $-\theta$ cause extrinsic spin-polarization effects [23].

### B. Rashba splitting of image-potential state

The IPE data presented in Fig. 1 showed additional surface-related features, the image states labeled IS just below the vacuum level. Figure 5(a) displays angle-resolved IPE spectra with improved statistics and a smaller step width (50 meV) for $-7.5° \leqslant \theta \leqslant 10.5°$ along $\overline{\Gamma}\,\overline{\mathrm{K}}$ in a limited energy interval where IS appears. Due to the finite experimental energy resolution, only the first member $n = 1$ of the Rydberg series is resolved. For $|\theta| \gtrsim 10°$, the intensity of IS fades. At the respective parallel momenta, IS overlaps with bulk states and becomes a surface resonance due to hybridization with bulk states [see Fig. 5(b)]. The linewidths of the $n = 1$ emissions are dominated by the apparatus function. To determine the peak positions, we fitted the spectra with Gaussian functions by using various types of backgrounds: (i) a constant background, and (ii) a linearly increasing background plus a falling edge of the bulk contribution at lower energies. The latter was used for the data points in Figs. 5(b) and 5(c). We want to emphasize that the deviations in the absolute energy positions for different backgrounds do not affect, within the uncertainty intervals, the values for effective mass and binding energy.

The parabolic-like dispersion of the IS around $\overline{\Gamma}$ is evident from Fig. 5(b), where the peak positions of the angle-resolved IPE spectra in Fig. 5(a) are transferred to an $E(\mathbf{k}_{\|})$ plot as orange circles. The surface-projected bulk band structure is indicated by the blue-shaded areas. The parabolic dispersion behavior is analyzed in Fig. 5(c), which shows a close-up of Fig. 5(b). A parabolic fit to the data (orange circles with uncertainty margins) yields an effective mass of $m^*/m_{\mathrm{e}} = 1.2 \pm 0.1$ (black solid line with $1\sigma$ uncertainty margins of the fit given by the gray shading). For comparison, the free-electron parabola is included as a dashed line. Clearly, the IS appears in a gap of the projected bulk band structure below the vacuum level $E_{\mathrm{V}}$. The vertex of the parabola is located at $E - E_{\mathrm{F}} = 4.66 \pm 0.02$ eV, i.e., at a binding energy of $E_{\mathrm{V}} - E = 0.68 \pm 0.04$ eV. According to a simple one-dimensional phase shift model, the binding energies of the IS depend on the energetic positions within the gap. For $n = 1$, the binding energy is calculated to be 0.85 eV for states at the top of the gap and 0.38 eV at the bottom of the gap [24,27]. In our case, the $n = 1$ state appears in the lower part of the gap, and in qualitative agreement with the model prediction, the binding energy is reduced compared with the top value of 0.85 eV.

The rather small predicted Rashba-type spin splittings in the range of a few tens of meV in view of an overall experimental energy resolution in IPE of about 400 meV set the stage for a challenging, but not hopeless, experiment. Since the partial spin spectra are measured separately, the detection of spin-dependent energy differences is not limited by the energy resolution but rather by the apparatus stability, statistics, and line shapes. Spin splittings (caused by exchange or spin-orbit interaction) of less than 20 meV have already been unambiguously detected via spin-resolved IPE [57,58].

Our spin- and angle-resolved IPE results for the $n = 1$ IS at Re(0001) are displayed in Fig. 6. Figure 6(a) shows the spin-resolved spectra for $-7.5^\circ \leqslant \theta \leqslant 8.5^\circ$ in the $\overline{\Gamma}\,\overline{\mathrm{K}}$ azimuth, where red up-pointing (blue down-pointing) triangles denote excitation with spin-up (spin-down) electrons. [The spectra for $\theta = 10.5^\circ$ are not taken into account due to the low signal-to-background intensity; see Fig. 5(a).] To extract a possible spin splitting $\Delta E_{\downarrow\uparrow}$ of the IS, we determined the peak positions of spin-up and spin-down emissions by a least-squares fitting procedure. This is not a trivial task given the statistical scatter of the data, the influence of the falling edge of the bulk emission on the low-energy side of the IS, the uncertainty about the energy dependence of the background intensity, the influence of the higher members of the IS Rydberg series, and the steplike background increase at $E_V$ due to continuum states. Therefore, we tested different energy intervals for the fits and different slopes for linear backgrounds. The slope of the assumed background intensity influences the deduced peak positions systematically. Therefore, the same background slope has to be used for both spin spectra in order to avoid artificial spin splittings. Since there is, on the low-energy side of the IS, decreasing intensity from the bulk emission and, on the high-energy side of the IS, increasing intensity due to inelastic secondary processes, a reasonable assumption for the fitting is a constant background intensity underlying the IS emission.

We illustrate our approach for the $\theta = 6.5^\circ$ spectra, shown as a close-up in Fig. 6(b). Note that the two partial spin spectra are shifted along the vertical axis for better visibility. The Gaussian fits to the data are shown as red and blue solid lines through the data points. The energy interval chosen for the fitting procedure is indicated by the solid symbols compared with the open symbols for data points that were not included in the fit. The blue and red vertical lines denote the determined peak positions of the fit functions, resulting in a sizable spin-dependent energy splitting. To determine and illustrate the uncertainty margins of the peak positions, we produced a series of 100 000 pseudoexperimental spectra by varying each measured data point randomly, corresponding to the Gaussian distribution of its own statistical uncertainty [see uncertainty margins in Fig. 6(b)]; for details see [57,58]. For each of the pseudoexperimental spectra we applied our fitting procedure. Figure 6(c) presents the resulting peak position distributions for all these pseudoexperimental spectra, for both spin up and spin down, which generates an easily interpretable graphic image of the spin splitting and its confidence interval: $\Delta E_{\downarrow\uparrow} = 43 \pm 23$ meV. Furthermore, the somewhat overlapping peak position distributions show that there is a probability of about 80% that IS is spin split at an angle of electron incidence of $\theta = 6.5^\circ$.

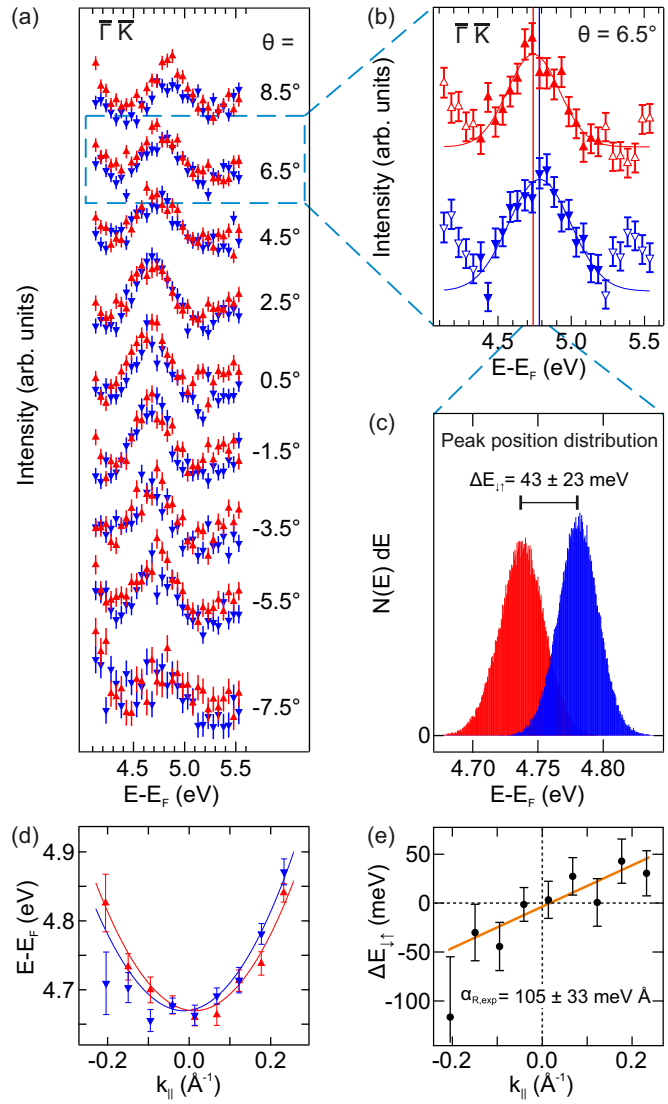


FIG. 6. (a) Spin- and angle-resolved IPE spectra of IS at Re(0001) along $\overline{\Gamma}\,\overline{\mathrm{K}}$. Red (blue) triangles indicate spin up (spin down). (b) Enlarged presentation of the spectra for $\theta = 6.5^\circ$ with Gaussian fits to the data within a limited energy interval indicated by filled data points. The vertical red and blue lines mark the spin-dependent peak positions as obtained from the fit. (c) Histogram of peak positions obtained from fitting 100 000 pseudospectra (see text for details), yielding a spin-dependent energy splitting of $\Delta E_{\downarrow\uparrow} = 43 \pm 23$ meV. (d) $E(\mathbf{k}_\parallel)$ diagram of the spin-dependent peak positions of IS derived from the spectra in (a). The red and blue lines are parabolic fits to the data. (e) $\Delta E_{\downarrow\uparrow}$ obtained from (d) as a function of $\mathbf{k}_\parallel$. A linear fit to the data results in a Rashba parameter $\alpha_{\mathrm{R,exp}} = 105 \pm 33$ meV Å.

We applied the described analysis to all spectra of the series shown in Fig. 6(a). The obtained spin-dependent energy positions of the IS and the resulting spin splittings $\Delta E_{\downarrow\uparrow}$ are plotted as a function of $k_\parallel$ in Figs. 6(d) and 6(e), respectively. Parabolic fits to the data in Fig. 6(d) provide evidence for Rashba-type behavior of the IS which is further supported by the linear behavior of $\Delta E_{\downarrow\uparrow}(k_\parallel)$ [see the orange straight line in Fig. 6(e)]. Note that the Gaussian fits to the pseudoexperimental spectra are stable against reasonable variations of

the fitting intervals and yield results within the uncertainties shown in Figs. 6(d) and 6(e).

Our resulting $\Delta E_{\downarrow\uparrow}(\mathbf{k}_\parallel)$ data show a linear trend for the spin splittings with a sign reversal around $\overline{\Gamma}$. A fit to the data yields a Rashba parameter of $\alpha_{\mathrm{R,exp}} = 105 \pm 33\,\mathrm{meV\,Å}$. Our data provide experimental evidence of a Rashba-type spin splitting of the IS directly by spin-resolved measurements. The experimental value for Re(0001) differs significantly from zero and is in qualitative agreement with theoretical results for other surfaces of high-$Z$ materials. The quantitative differences might partly be caused by the different materials and can partly be ascribed to shortcomings of the model potential which includes not uniquely fixed parameters.

## IV. CONCLUSION

We studied the unoccupied electronic structure of Re(0001) theoretically and experimentally by spin- and angle-resolved IPE. Along the high-symmetry azimuths $\overline{\Gamma}\,\overline{\mathrm{K}}$ and $\overline{\Gamma}\,\overline{\mathrm{M}}$, bulk- and surface-related states have been identified which are in good agreement with state-of-the-art DFT calculations. A Rashba-split hole pocket of a surface state around $\overline{\Gamma}$ finds continuation for larger $k_\parallel$ values in both azimuths, where the surface state appears again above the Fermi level and forms a W-shaped state. The Rashba-type spin splitting of these states is confirmed by spin-resolved measurements. IPE measurements with varying photon-detection angles show that the dipolar axes of the transitions are oriented normal to the surface, indicative of $z$-type orbital character ($p_z$, $d_{z^2}$) of the respective surface states.

Furthermore, the image-potential surface states have been identified and studied as a function of $\mathbf{k}_\parallel$. We observed the expected free-electron-like dispersion behavior with a binding energy of $E_\mathrm{V} - E = 0.68 \pm 0.04\,\mathrm{eV}$ and an effective mass of $m^*/m_e = 1.2 \pm 0.1$. Spin-resolved measurements provide direct evidence of a spin-orbit-induced Rashba-type behavior of the image state with a Rashba parameter of $\alpha_{\mathrm{R,exp}} = 105 \pm 33\,\mathrm{meV\,Å}$. *Ab initio* descriptions of the image states under the influence of spin-orbit interaction are numerically very challenging. Details of the small overlap of the image state wave function with the surface region are essential for the size of spin-orbit-induced image-state splittings. To improve the theoretical modeling, reliable experimental data beyond the determination of binding energies and effective masses are mandatory. This work and future spin-resolved IPE as well as 2PPE investigations on Rashba parameters for image states on various high-$Z$ surfaces will provide the necessary input.

## ACKNOWLEDGMENTS

We thank J. Braun, M. Holtmann, and J. Minár for fruitful discussions.

[1] R. Feder, *Polarized Electrons in Surface Physics* (World Scientific, Singapore, 1995).

[2] U. Heinzmann and J. H. Dil, Spin-orbit-induced photoelectron spin polarization in angle-resolved photoemission from both atomic and condensed matter targets, J. Phys.: Condens. Matter **24**, 173001 (2012).

[3] T. Okuda and A. Kimura, Spin- and angle-resolved photoemission of strongly spin-orbit coupled systems, J. Phys. Soc. Jpn. **82**, 021002 (2013).

[4] S. LaShell, B. A. McDougall, and E. Jensen, Spin Splitting of an Au(111) Surface State Band Observed with Angle Resolved Photoelectron Spectroscopy, Phys. Rev. Lett. **77**, 3419 (1996).

[5] M. Hoesch, M. Muntwiler, V. N. Petrov, M. Hengsberger, L. Patthey, M. Shi, M. Falub, T. Greber, and J. Osterwalder, Spin structure of the Shockley surface state on Au(111), Phys. Rev. B **69**, 241401(R) (2004).

[6] A. Varykhalov, D. Marchenko, M. R. Scholz, E. D. L. Rienks, T. K. Kim, G. Bihlmayer, J. Sánchez-Barriga, and O. Rader, Ir(111) Surface State with Giant Rashba Splitting Persists under Graphene in Air, Phys. Rev. Lett. **108**, 066804 (2012).

[7] S. N. P. Wissing, C. Eibl, A. Zumbülte, A. B. Schmidt, J. Braun, J. Minár, H. Ebert, and M. Donath, Rashba-type spin splitting at Au(111) beyond the Fermi level: The other part of the story, New J. Phys. **15**, 105001 (2013).

[8] K. T. Ritter, K. Miyamoto, T. Okuda, and M. Donath, Rashba-type splitting of the Au(110) surface state: A combined inverse and direct photoemission study, Phys. Rev. B **104**, L161101 (2021).

[9] M. Hochstrasser, J. G. Tobin, E. Rotenberg, and S. D. Kevan, Spin-Resolved Photoemission of Surface States of W(110)-(1 × 1)H, Phys. Rev. Lett. **89**, 216802 (2002).

[10] K. Miyamoto, A. Kimura, K. Kuroda, T. Okuda, K. Shimada, H. Namatame, M. Taniguchi, and M. Donath, Spin-Polarized Dirac-Cone-Like Surface State with $d$ Character at W(110), Phys. Rev. Lett. **108**, 066808 (2012).

[11] K. Miyamoto, A. Kimura, T. Okuda, K. Shimada, H. Iwasawa, H. Hayashi, H. Namatame, M. Taniguchi, and M. Donath, Massless or heavy due to two-fold symmetry: Surface-state electrons at W(110), Phys. Rev. B **86**, 161411(R) (2012).

[12] H. Wortelen, K. Miyamoto, H. Mirhosseini, T. Okuda, A. Kimura, D. Thonig, J. Henk, and M. Donath, Spin-orbit influence on $d_{z^2}$-type surface state at Ta(110), Phys. Rev. B **92**, 161408(R) (2015).

[13] B. Engelkamp, H. Wortelen, H. Mirhosseini, A. B. Schmidt, D. Thonig, J. Henk, and M. Donath, Spin-polarized surface electronic structure of Ta(110): Similarities and differences to W(110), Phys. Rev. B **92**, 085401 (2015).

[14] D. Kutnyakhov, S. Chernov, K. Medjanik, R. Wallauer, C. Tusche, M. Ellguth, S. A. Nepijko, M. Krivenkov, J. Braun, S. Borek, J. Minár, H. Ebert, H. J. Elmers, and G. Schönhense, Spin texture of time-reversal symmetry invariant surface states on W(110), Sci. Rep. **6**, 29394 (2016).

[15] H. J. Elmers, D. Kutnyakhov, S. Chernov, K. Medjanik, O. Fedchenko, A. Zaporozhchenko-Zymakova, M. Ellguth, D. Tusche, J. Viefhaus, and G. Schönhense, Hosting of surface states in spin-orbit induced projected bulk band gaps of W(110) and Ir(111), J. Phys.: Condens. Matter **29**, 255001 (2017).

[16] A. Varykhalov, D. Marchenko, J. Sánchez-Barriga, E. Golias, O. Rader, and G. Bihlmayer, Tilted Dirac cone on W(110) protected by mirror symmetry, Phys. Rev. B **95**, 245421 (2017).

[17] H. Mirhosseini, M. Flieger, and J. Henk, Dirac-cone-like surface state in W(110): Dispersion, spin texture and

photoemission from first principles, New J. Phys. **15**, 033019 (2013).

[18] J. Braun, K. Miyamoto, A. Kimura, T. Okuda, M. Donath, H. Ebert, and J. Minár, Exceptional behavior of d-like surface resonances on W(110): The one-step model in its density matrix formulation, New J. Phys. **16**, 015005 (2014).

[19] D. Thonig, T. Rauch, H. Mirhosseini, J. Henk, I. Mertig, H. Wortelen, B. Engelkamp, A. B. Schmidt, and M. Donath, Existence of topological nontrivial surface states in strained transition metals: W, Ta, Mo, and Nb, Phys. Rev. B **94**, 155132 (2016).

[20] A. Urru and A. Dal Corso, Clean Os(0001) electronic surface states: A first-principle fully relativistic investigation, Surface Sci. **671**, 17 (2018).

[21] A. Urru and A. Dal Corso, Spin-polarized electronic surface states of Re(0001): An ab-initio investigation, Surface Sci. **686**, 22 (2019).

[22] H. J. Elmers, J. Regel, T. Mashoff, J. Braun, S. Babenkov, S. Chernov, O. Fedchenko, K. Medjanik, D. Vasilyev, J. Minar, H. Ebert, and G. Schönhense, Rashba splitting of the Tamm surface state on Re(0001) observed by spin-resolved photoemission and scanning tunneling spectroscopy, Phys. Rev. Research **2**, 013296 (2020).

[23] S. Schemmelmann, P. Krüger, F. Schöttke, and M. Donath, Rashba-split surface state and spin-dependent photon emission from Re(0001) at $\overline{\Gamma}$, Phys. Rev. B **104**, 205425 (2021).

[24] P. M. Echenique and J. B. Pendry, Theory of image states at metal surfaces, Prog. Surface Sci. **32**, 111 (1989).

[25] P. M. Echenique, R. Berndt, E. V. Chulkov, T. Fauster, A. Goldmann, and U. Höfer, Decay of electronic excitations at metal surfaces, Surface Sci. Rep. **52**, 219 (2004).

[26] V. Dose, W. Altmann, A. Goldmann, U. Kolac, and J. Rogozik, Image-potential States Observed by Inverse Photoemission, Phys. Rev. Lett. **52**, 1919 (1984).

[27] T. Fauster, Quantization of electronic states on metal surfaces, Appl. Phys. A **59**, 479 (1994).

[28] M. Weinelt, Time-resolved two-photon photoemission from metal surfaces, J. Phys.: Condens. Matter **14**, R1099 (2002).

[29] M. Donath, C. Math, M. Pickel, A. B. Schmidt, and M. Weinelt, Realization of a spin-polarized two-dimensional electron gas via image-potential-induced surface states, Surface Sci. **601**, 5701 (2007).

[30] J. R. McLaughlan, E. M. Llewellyn-Samuel, and S. Crampin, Spin-orbit splitting of image states, J. Phys.: Condens. Matter **16**, 6841 (2004).

[31] Y. A. Bychkov and E. I. Rashba, Properties of a 2D electron gas with lifted spectral degeneracy, Pis'ma Zh. Eksp. Teor. Fiz. **39**, 66 (1984) [JETP Lett. **39**, 78 (1984)].

[32] A. Nuber, J. Braun, F. Forster, J. Minár, F. Reinert, and H. Ebert, Surface versus bulk contributions to the Rashba splitting in surface systems, Phys. Rev. B **83**, 165401 (2011).

[33] J. Braun and H. Ebert, The impact of spin–orbit interaction on the image states of high–Z materials, Phys. Status Solidi B **258**, 2000026 (2020).

[34] S. Tognolini, S. Achilli, L. Longetti, E. Fava, C. Mariani, M. I. Trioni, and S. Pagliara, Rashba Spin-Orbit Coupling in Image Potential States, Phys. Rev. Lett. **115**, 046801 (2015).

[35] R. Arafune, T. Nakazawa, N. Takagi, M. Kawai, and H. Ishida, Comment on "Rashba Spin-Orbit Coupling in Image Potential States," Phys. Rev. Lett. **117**, 239701 (2016).

[36] S. Tognolini, S. Achilli, L. Longetti, E. Fava, C. Mariani, M. I. Trioni, and S. Pagliara, Tognolini *et al.* Reply: Phys. Rev. Lett. **117**, 239702 (2016).

[37] T. Nakazawa, N. Takagi, M. Kawai, H. Ishida, and R. Arafune, Rashba splitting in an image potential state investigated by circular dichroism two-photon photoemission spectroscopy, Phys. Rev. B **94**, 115412 (2016).

[38] R. Arafune, N. Takagi, and H. Ishida, Spin-orbit interaction in unoccupied surface states, Prog. Surface Sci. **93**, 177 (2018).

[39] B. Kim, C. H. Kim, P. Kim, W. Jung, Y. Kim, Y. Koh, M. Arita, K. Shimada, H. Namatame, M. Taniguchi, J. Yu, and C. Kim, Spin and orbital angular momentum structure of Cu(111) and Au(111) surface states, Phys. Rev. B **85**, 195402 (2012).

[40] H. Ryu, I. Song, B. Kim, S. Cho, S. Soltani, T. Kim, M. Hoesch, C. H. Kim, and C. Kim, Photon energy dependent circular dichroism in angle-resolved photoemission from Au(111) surface states, Phys. Rev. B **95**, 115144 (2017).

[41] M. Donath, Spin-dependent electronic structure at magnetic surfaces: The low-Miller-index surfaces of nickel, Surface Sci. Rep. **20**, 251 (1994).

[42] S. D. Stolwijk, H. Wortelen, A. B. Schmidt, and M. Donath, Rotatable spin-polarized electron source for inverse-photoemission experiments, Rev. Sci. Instrum. **85**, 013306 (2014).

[43] M. Donath, Spin-resolved inverse photoemission of ferromagnetic surfaces, Appl. Phys. A **49**, 351 (1989).

[44] A. Zumbülte, A. B. Schmidt, and M. Donath, Momentum resolution in inverse photoemission, Rev. Sci. Instrum. **86**, 013908 (2015).

[45] M. Budke, T. Allmers, M. Donath, and G. Rangelov, Combined experimental setup for spin- and angle-resolved direct and inverse photoemission, Rev. Sci. Instrum. **78**, 113909 (2007).

[46] C. Thiede, A. B. Schmidt, and M. Donath, Optimizing the performance of bandpass photon detectors for inverse photoemission: Transmission of alkaline earth fluoride window crystals, Rev. Sci. Instrum. **86**, 085101 (2015).

[47] C. Thiede, I. Niehues, A. B. Schmidt, and M. Donath, The acetone bandpass detector for inverse photoemission: Operation in proportional and Geiger–Müller modes, Meas. Sci. Technol. **29**, 065901 (2018).

[48] M. Budke, V. Renken, H. Liebl, G. Rangelov, and M. Donath, Inverse photoemission with energy resolution better than 200 meV, Rev. Sci. Instrum. **78**, 083903 (2007).

[49] J. P. Perdew and A. Zunger, Self-interaction correction to density-functional approximations for many-electron systems, Phys. Rev. B **23**, 5048 (1981).

[50] P. Schröer, P. Krüger, and J. Pollmann, First-principles calculation of the electronic structure of the wurtzite semiconductors ZnO and ZnS, Phys. Rev. B **47**, 6971 (1993).

[51] D. R. Hamann, Generalized norm-conserving pseudopotentials, Phys. Rev. B **40**, 2980 (1989).

[52] B. Stärk, P. Krüger, and J. Pollmann, Magnetic anisotropy of thin Co and Ni films on diamond surfaces, Phys. Rev. B **84**, 195316 (2011).

[53] L. Kleinman and D. M. Bylander, Efficacious Form for Model Pseudopotentials, Phys. Rev. Lett. **48**, 1425 (1982).

[54] M. Donath, M. Glöbl, B. Senftinger, and V. Dose, Photon polarization effects in inverse photoemission from Cu(001), Solid State Commun. **60**, 237 (1986).

[55] T. Fauster, R. Schneider, and H. Dürr, Angular distribution of the inverse photoemission from Cu(100), Phys. Rev. B **40**, 7981 (1989).

[56] E. E. Krasovskii and E. V. Chulkov, Rashba polarization of bulk continuum states, Phys. Rev. B **83**, 155401 (2011).

[57] F. Passek and M. Donath, Spin-Split Image-Potential-Induced Surface State on Ni(111), Phys. Rev. Lett. **69**, 1101 (1992).

[58] P. Eickholt, C. Sanders, M. Dendzik, L. Bignardi, D. Lizzit, S. Lizzit, A. Bruix, P. Hofmann, and M. Donath, Spin Structure of K Valleys in Single-Layer $WS_2$ on Au(111), Phys. Rev. Lett. **121**, 136402 (2018).